

1 **A theoretical model of fuselage pressure levels**
2 **due to fan tones radiated from the intake of**
3 **an installed turbofan aero-engine**

4 James Gaffney and Alan McAlpine

Institute of Sound and Vibration Research, University of Southampton, Southampton, SO17 1BJ, UK

Michael J. Kingan

Department of Mechanical Engineering, University of Auckland, Auckland, New Zealand

5 May 23, 2018

Abstract

An existing theoretical model to predict the pressure levels on an aircraft's fuselage is improved by incorporating a more physically realistic method to predict fan tone radiation from the intake of an installed turbofan aero-engine. Such a model can be used as part of a method to assess cabin noise. Fan tone radiation from a turbofan intake is modelled using the exact solution for the radiated pressure from a spinning mode exiting a semi-infinite cylindrical duct immersed in a uniform flow. This approach for a spinning duct mode incorporates scattering/diffraction by the intake lip, enabling predictions of the radiated pressure valid in both the forward and aft directions. The aircraft's fuselage is represented by an infinitely long, rigid cylinder. There is uniform flow aligned with the cylinder, except close to the cylinder's surface where there is a constant-thickness boundary layer. In addition to single mode calculations it is shown how the model may be used to rapidly calculate a multi-mode incoherent radiation from the engine intake. Illustrative results are presented which demonstrate the relative importance of boundary-layer shielding both upstream and downstream of the source, as well as examples of the fuselage pressure levels due to a multi-mode tonal source at high Helmholtz number.

23 I. Introduction

24 In modern civil aircraft, turbofan jet engines are the dominant noise source during take-off
25 and cruise. Successive legislative and certification requirements have set stringent targets
26 for reductions in noise emissions from civil aircraft. Reducing the impact of aircraft noise
27 requires reliable and fast noise prediction tools which can be used for engineering optimisation
28 studies during the development of new quieter engines. Owing to the complexity of the
29 turbomachinery, it is routine to separately predict the sound radiation from individual sources
30 (such as the fan, turbine and jet). Normally the sound radiation is modelled in the free field,
31 but in reality sound radiation can be affected by the airframe.

32 Installation acoustics for turbofan jet engines refers to the study of how the radiated noise
33 is affected when an engine is installed on an airframe. Of particular relevance is the pressure
34 levels on the aircraft's fuselage since the sound transmitted through the fuselage will directly
35 affect the cabin noise levels. Fan tones radiating from an engine intake duct, particularly
36 "buzz-saw" tones which are produced when the fan tip speed is supersonic, can radiate at
37 very high pressure amplitudes. Predicting the pressure levels on the fuselage surface is required
38 in order to assess what acoustic treatments must be applied in order to achieve an acceptable
39 cabin noise level.

40 In this theoretical model, the source or incident field represents a fan tone radiated from
41 a turbofan intake. Adjacent to the intake, an infinitely long, rigid cylinder represents a
42 cylindrical fuselage. The scattering method can be used to determine the pressure field
43 everywhere, albeit in this work attention is focussed on the pressure levels on the cylinder.

44 The solution of the scattered field due to an acoustic monopole located adjacent to an

45 infinite, rigid cylinder in a stationary fluid is given in the text by Bowman, Senior and
46 Uslenghi ([1], Chapter 2, Sec. 2.5.2, pp. 126–127). By solving the convected wave equation
47 rather than the wave equation, the solution for the scattered field in the presence of a uniform
48 axial flow aligned with the cylinder axis can also be derived. However, for the purpose of
49 modelling sound propagation from the engine intake to the fuselage surface, the effect of
50 refraction within the fuselage boundary layer must be taken into account. Sound propagating
51 upstream is refracted away from the surface of the fuselage by the boundary layer, which is
52 referred to as ‘shielding’. Early examples of this include McAninch [2] and Hanson [3] with
53 studies of a monopole over a flat plate with a boundary layer. Following this, a significant
54 advance was presented by Hanson and Magliozzi [4] who developed an installation acoustics
55 model of a propeller-type source located adjacent to an infinite, rigid cylinder in the presence
56 of an axial mean flow including a boundary layer on the cylinder. Later, Lu [5] added a
57 temperature gradient to the boundary layer, although this was found to be inconsequential
58 on the shielding. More recently, Belyaev [6] and Brouwer [7] studied the effects of installed
59 open-rotor engines. Generally, all these papers found that significant shielding can be caused
60 by the boundary layer upstream of the source, thereby reducing the pressure levels on the
61 surface of the fuselage, but the shielding and effect on the pressure levels caused by the
62 boundary layer is minimal downstream of the source.

63 There is far less research on fan tone sources radiated from turbofan aero-engines, and the
64 resulting fuselage pressure levels. Siefert and Delfs [8] and Dierke et al. [9] have employed
65 Computational Aero-Acoustics (CAA) methods to predict the scattering and refraction by
66 the fuselage of a spinning mode radiated from a turbofan intake duct. The computational
67 method was also able to examine the effect of spectral broadening.

68 The current article is a continuation of theoretical work by the authors [10],[11] on pre-
69 diction of the fuselage pressure levels due to intake fan tone radiation. In McAlpine, Gaffney
70 and Kingan [10] the pressure levels on a cylindrical fuselage forward of the intake duct were
71 simulated using a theoretical solution based on an incident field given by a distributed “disk”
72 acoustic source located adjacent to an infinite, rigid cylinder. The disk source derivation was
73 based on the Rayleigh integral adopted by Tyler and Sofrin [12]. In this earlier work, the mean
74 flow was taken to be a uniform axial flow aligned with the axis of the cylinder. Subsequently,
75 this theoretical solution was extended by Gaffney, McAlpine and Kingan [11] to include the
76 fuselage boundary layer. This requires the numerical solution of the Pridmore-Brown equa-
77 tion in the boundary-layer region which is matched to the solution for the convected wave
78 equation (uniform flow) at the edge of the boundary layer.

79 The key advancement in the current article is to use the full Wiener–Hopf solution for a
80 spinning mode exiting a cylindrical duct, instead of the disc source, to specify the incident
81 field. The Wiener–Hopf solution gives the pressure radiated into a free field. It is shown how
82 to combine this solution with the cylindrical fuselage scattering method. Combining these
83 two existing methods gives a theoretical installation acoustics model for intake fan noise, with
84 an adjacent cylindrical fuselage in the near field, and inclusion of the fuselage boundary-layer
85 which can shield the forward radiated fan noise. Thus new results in this article focus on the
86 predicted shielding effect of the boundary layer for intake fan tone radiation. Additionally
87 it is shown how to use the model to rapidly calculate a multi-mode incoherent source, as
88 opposed to calculations for the radiation of a single mode.

89 The benefit of using the incident field given by the Wiener–Hopf solution for a spinning
90 mode incorporates scattering/diffraction by the intake lip, and accounts for reflection of sound

91 at the exit plane of the intake. Thus it provides a more realistic incident field compared to
92 the disk source model which does not account for the effects of the intake duct. The other
93 key benefit of using the incident field given by the Wiener–Hopf solution for a spinning mode
94 is that predictions will be more realistic near the source plane ($\theta = 90^\circ$), and can be extended
95 to downstream ($\theta > 90^\circ$). This is not possible with the disk source model whose predictions
96 only will be realistic up to a maximum polar angle, say θ_{\max} , where $\theta_{\max} < 90^\circ$.

97 The overall situation is shown sketched in Fig. 1 which illustrates for wing-mounted engines
98 the intake fan noise installation acoustics model. Both forward and aft radiated fan noise from
99 modern turbofan aero-engines are significant contributors to the overall noise. Modelling
100 radiation of fan noise from the bypass duct increases the complexity of the prediction method
101 because it is necessary to model the noise propagating through the exhaust jet shear layers.
102 Additionally there are other significant contributors to the aft radiated noise such as core,
103 turbine and jet noise sources, and for engines mounted under the wings, the propagation and
104 radiation of exhaust noise will be affected by the wings.

105 Consequently, it is assumed that noise radiated from the intake which is incident on the
106 fuselage is the dominant source forward of the aircraft wings, but it is expected that down-
107 stream of the wings, the exhaust noise sources would be required for realistic predictions of
108 the fuselage pressure levels. Thus, although the Wiener–Hopf solution is valid at all polar
109 angles, i.e. both upstream and downstream, it is emphasised that further downstream the
110 fuselage pressure levels will be dominated by exhaust noise sources. Without predicting the
111 levels of other (exhaust) noise sources, the maximum polar angle at which the intake fan
112 noise radiation is the dominant source cannot be precisely quantified. As shown in Fig. 1,
113 the polar range over which the intake fan noise method should be reasonably applied, using

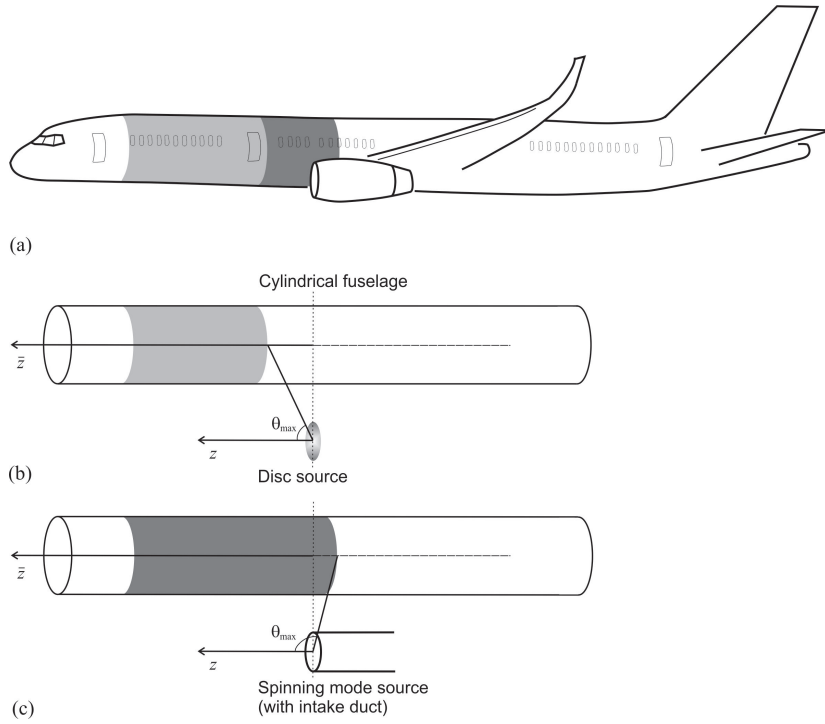


Figure 1: Canonical problem for intake fan tone radiation from an installed turbofan aero-engine. (a) Sketch of an installed turbofan aero-engine mounted below the wings. (b) Incident field = disk source. (c) Incident field = Spinning mode. Polar angle θ_{max} indicates, along with the shaded regions, roughly where predictions of the fuselage pressure levels are valid.

114 either the disk source or the spinning mode source to specify the incident field, is illustrated.
 115 This illustrates the significant increase in the area of the fuselage where predictions of the
 116 pressure levels can be applied using the Wiener–Hopf solution for a spinning mode, compared
 117 to utilising the disk source for the incident field. In this work, the focus is intake fan tone
 118 noise, predominantly “buzz-saw” tones, incident on this portion of the fuselage forward of the
 119 wings.

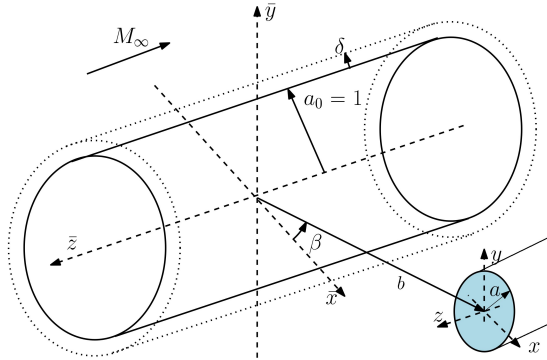


Figure 2: (Color online) Sketch of the cylindrical fuselage (radius a_0) and the circular intake duct (radius a). The centreline of the cylinder is aligned with the \bar{z} -axis. The intake duct is aligned with the z -axis, and the duct termination is located in the plane $z = \bar{z} = 0$. The transverse distance between the centre of the intake duct and the centre of the cylinder is b .

Also shown is the edge of the fuselage boundary-layer (thickness δ).

120 II. Theory

121 A sketch of the problem set-up is shown in Fig. 2. The Cartesian reference frame for the
 122 intake is (x, y, z) , or equivalently in cylindrical polar coordinates (r, ϕ, z) , where the centre of
 123 the intake is aligned with the z -axis, and the duct termination is at $z = 0$. The Cartesian
 124 reference frame for the fuselage is $(\bar{x}, \bar{y}, \bar{z})$, or equivalently in cylindrical polar coordinates
 125 $(\bar{r}, \bar{\phi}, \bar{z})$. There is a subsonic uniform mean flow, Mach number M_∞ , directed in the negative
 126 \bar{z} -direction. Also there is a fuselage boundary layer with constant thickness δ .

127 In the following analysis, all values are dimensionless: the reference length scale is equal
 128 to the fuselage radius a_0 ; the reference velocity is the speed of sound c_0 ; the reference density
 129 is ρ_0 , and the pressure is scaled by $\rho_0 c_0^2$.

130 The principal difference between the theory in this article compared to the theory presented

131 in Gaffney, McAlpine and Kingan [11] is the method to calculate the incident field. In the
 132 previous article [11], fan tone radiation from an intake is represented by a disk source model.
 133 In the current article, fan tone radiation is calculated using the Wiener–Hopf solution for a
 134 spinning mode radiated from a cylindrical intake duct. This solution was given by Homicz
 135 and Lordi in 1975 [13], albeit we have used a more recent formulation taken from Gabard
 136 and Astley [14] which itself was based on the formulation by Munt [16]. Subsequently the
 137 procedure to calculate the scattered field, and to construct the total field, is the same as
 138 detailed in Gaffney, McAlpine and Kingan ([11], Sec. II). Accordingly, in this article, only
 139 the theory for the incident field is covered in detail, and for brevity, only brief details are
 140 given about the procedure to calculate the fuselage scattering including the boundary-layer
 141 refraction.

142 **A. In-duct Sound Field**

143 The intake is modelled by a cylindrical duct with a rigid, impervious and infinitesimal wall.
 144 The duct has radius a and is semi-infinite, $-\infty < z < 0$. The flow velocity inside the duct
 145 is the same as the flow outside the duct, i.e. Mach number M_∞ directed in the negative
 146 z -direction. It is also noted that the ambient density ρ_0 , and speed of sound c_0 are uniform
 147 everywhere.

148 The in-duct acoustic pressure field is defined in terms of spinning modes [12]. Each mode
 149 is defined by its integer azimuthal order l and radial order q . Time-harmonic solutions are
 150 expressed by $p_{lq} = \hat{p}_{lq}(r, z) \exp \{i(\omega_0 t - l\phi)\}$ and $u_{zlq} = \hat{u}_{zlq}(r, z) \exp \{i(\omega_0 t - l\phi)\}$ for the
 151 acoustic pressure and axial particle velocity respectively, noting that the values are normalised

152 such that $k_0 = \omega_0$. These are found by solving the convected Helmholtz equation, which gives

$$\hat{p}_{lq}(r, z) = P_{lq} J_l(\kappa_{lq} r) e^{-ik_{z lq} z}, \quad (1)$$

$$\hat{u}_{z lq}(r, z) = \xi_{lq} P_{lq} J_l(\kappa_{lq} r) e^{-ik_{z lq} z}, \quad (2)$$

153 where P_{lq} is the modal amplitude, $J_l(\cdot)$ denotes the Bessel function of the first kind of order
 154 l , and $\kappa_{lq}, k_{z lq}$ denote the radial and axial wavenumber of mode (l, q) respectively. The rigid
 155 boundary condition on the duct wall gives the radial wavenumber which corresponds to the
 156 l^{th} turning point of the Bessel function. The acoustic pressure and particle velocity are linked
 157 via the factor

$$\xi_{lq} = \frac{k_{z lq}}{k_0 + k_{z lq} M_\infty}, \quad (3)$$

158 and the dispersion relationship (valid for the in-duct field) is given by

$$k_{z lq}^2 + \kappa_{lq}^2 = (k_0 + k_{z lq} M_\infty)^2. \quad (4)$$

159 The modal amplitude can be related to the modal power W_{lq} via

$$|P_{lq}| = \sqrt{\frac{2W_{lq}}{\pi [a^2 - (l/\kappa_{lq})^2] J_l^2(\kappa_{lq} a) \left[(1 + M_\infty^2) \text{Re} \{ \xi_{lq} \} - M_\infty (1 + |\xi_{lq}|^2) \right]}}. \quad (5)$$

160 This relation will be used to specify the amplitude of each mode to form an incoherent,
 161 equal-power-per-mode source for which illustrative examples are provided in Sec. IV.

162 B. Incident Field

163 The Wiener–Hopf formulation by Gabard and Astley [14] for a spinning mode radiated from
 164 a cylindrical duct is used to determine the incident field. The key parts of the derivation are
 165 outlined in this section. Full details and how to implement the solution are given in Ref. [14].

166 Differences between this and the formulation by Gabard and Astley is the convention for
 167 time-harmonic quantities and the choice of reference length scale*. Also Gabard and Astley
 168 derive the solution based on a velocity potential formulation, whereas in this article the key
 169 steps in the analysis are formulated in terms of the pressure.

170 The problem is defined such that the incident field \hat{p}_i for mode (l, q) is given by a summation
 171 of the (in-duct) spinning mode, given by Eq. (1), and a diffracted field \hat{p}_d , such that

$$\hat{p}_i = \begin{cases} \hat{p}_{lq} + \hat{p}_d & , \quad r < a \\ \hat{p}_d & , \quad r > a \end{cases} . \quad (6)$$

172 Since the walls of the duct have infinitesimal thickness, conditions are specified taking the
 173 limits as $r \rightarrow a^-$ and $r \rightarrow a^+$, where the superscript $-$ denotes approaching $r = a$ from
 174 $r < a$, and the superscript $+$ denotes approaching $r = a$ from $r > a$. In the region $z < 0$, this
 175 corresponds to taking the limit inside or outside the duct. Therefore, on the rigid duct wall
 176 the radial particle velocity is zero. This is equivalent to zero pressure gradient, i.e.

$$\frac{\partial \hat{p}_i(a^-, z)}{\partial r} = \frac{\partial \hat{p}_i(a^+, z)}{\partial r} = 0, \quad z < 0. \quad (7)$$

177 Forward of the duct, there is pressure continuity, i.e.

$$\hat{p}_i(a^-, z) = \hat{p}_i(a^+, z), \quad z \geq 0, \quad (8)$$

$$\Rightarrow \hat{p}_{lq}(a^-, z) + \hat{p}_d(a^-, z) = \hat{p}_d(a^+, z), \quad z \geq 0. \quad (9)$$

178 Therefore, the diffracted field must be discontinuous at $r = a$ for $z \geq 0$. The pressure

*Gabard and Astley define time-harmonic waves using the convention $\exp\{-i\omega_0 t\}$ and take the duct radius a as the reference lengthscale. In the current article, the convention used for time-harmonic waves is $\exp\{i\omega_0 t\}$ and the reference lengthscale is the cylinder radius a_0 .

179 jump in the diffracted field is

$$\Delta \hat{p}_d = \hat{p}_d(a^+, z) - \hat{p}_d(a^-, z) = \hat{p}_{lq}(a^-, z), \quad z \geq 0. \quad (10)$$

180 The solution is found by taking a Fourier transform in the axial position z , however, the
 181 Fourier transform is split into two half-range transforms to take account of the different
 182 boundary conditions on $r = a$ for $z < 0$ and $z \geq 0$, i.e.

$$\tilde{p}_{d-}(r, \bar{k}_z) = \int_{-\infty}^0 \hat{p}_d(r, z) e^{ik_0 \bar{k}_z z} dz, \quad (11a)$$

$$\tilde{p}_{d+}(r, \bar{k}_z) = \int_0^{\infty} \hat{p}_d(r, z) e^{ik_0 \bar{k}_z z} dz, \quad (11b)$$

183 where $\bar{k}_z = k_z/k_0$. The full transform is

$$\tilde{p}_d = \tilde{p}_{d-} + \tilde{p}_{d+}. \quad (12)$$

184 Following Gabard and Astley [14], it can be shown that $p_{d\pm}$ are regular in the half-planes R_{\pm}
 185 where $R_{\pm}: \mp \text{Im}(k_z - k_z^{\pm}) < \mp \tan(\epsilon) \text{Re}(k_z - k_z^{\pm})$.

186 Upon Fourier transformations the convected Helmholtz equation reduces to Bessel's differ-
 187 ential equation, and the solutions are chosen as

$$\tilde{p}_d(r, \bar{k}_z) = \begin{cases} A(\bar{k}_z) H_l^{(2)}(k_0 \Gamma_0 r) & r > a \\ B(\bar{k}_z) J_l(k_0 \Gamma_0 r) & r < a \end{cases}. \quad (13)$$

188 Note that $H_l^{(2)}(\cdot)$ is the Hankel function of the second kind of order l . This solution is
 189 selected for $r > a$ because it satisfies the appropriate radiation condition as $r \rightarrow \infty$ (outward
 190 propagating wave). The other solution with $J_l(\cdot)$ is selected for $r < a$ because it satisfies the
 191 finiteness condition at $r = 0$.

192 Outside of the duct the dispersion relationship is

$$\bar{k}_z^2 + \Gamma_0^2 = (1 + \bar{k}_z M_{\infty})^2. \quad (14)$$

193 This can be written as $\Gamma_0 = \Gamma_0^+ \Gamma_0^-$ where

$$\Gamma_0^+ = [1 + (M_\infty - 1)\bar{k}_z]^{1/2} \quad \text{and} \quad \Gamma_0^- = [1 + (M_\infty + 1)\bar{k}_z]^{1/2}, \quad (15)$$

194 where Γ_0^\pm have zeros at

$$\bar{k}_z^- = -\frac{1}{1 + M_\infty} \quad \text{and} \quad \bar{k}_z^+ = \frac{1}{1 - M_\infty}. \quad (16)$$

195 The transform of the radial particle displacement $\hat{\varepsilon}_r$ on $r = a$ by W . This reduces to the
196 half-range transform

$$W_+(\bar{k}_z) = \int_0^\infty \hat{\varepsilon}_r(a, z) e^{ik_0\bar{k}_z z} dz, \quad (17)$$

197 since the radial particle velocity is zero on the rigid duct, hence $W_- = 0$.

198 Then taking the transform of the radial component of the linearised momentum equation,
199 and substituting Eqs. (13) and (17), gives

$$(1 + \bar{k}_z M_\infty)^2 W_+ = A(\bar{k}_z) \Gamma_0 H_l^{(2)'}(k_0 \Gamma_0 a) = B(\bar{k}_z) \Gamma_0 J_l'(k_0 \Gamma_0 a). \quad (18)$$

200 The objective is to find $A(\bar{k}_z)$ and $B(\bar{k}_z)$ by deriving an expression for W_+ . The transform
201 of the pressure jump of the diffracted field [Eq. (10)] is

$$G(\bar{k}_z) = \int_{-\infty}^\infty \Delta \hat{p}_d e^{ik_0\bar{k}_z z} dz, \quad (19)$$

$$= \int_{-\infty}^\infty [\hat{p}_d(a^+, z) - \hat{p}_d(a^-, z)] e^{ik_0\bar{k}_z z} dz, \quad (20)$$

202 which, from Eq. (13), leads to

$$G(\bar{k}_z) = A(\bar{k}_z) H_l^{(2)}(k_0 \Gamma_0 a) - B(\bar{k}_z) J_l(k_0 \Gamma_0 a). \quad (21)$$

203 However, since the pressure is continuous on $r = a$ for $z > 0$, combining Eqs. (1), (10) and
204 (20), the positive half-range transform of G can be evaluated analytically,

$$G_+(\bar{k}_z) = P_{lq} \int_0^\infty J_l(\kappa_{lq} a) e^{-ik_z l q z} e^{ik_0\bar{k}_z z} dz = iP_{lq} \frac{J_l(\kappa_{lq} a)}{k_{z,lq} - k_0\bar{k}_z}. \quad (22)$$

205 Next, substituting for $A(\bar{k}_z)$ and $B(\bar{k}_z)$ from Eq. (18)

$$G(\bar{k}_z) = G_-(\bar{k}_z) + G_+(\bar{k}_z) = \frac{W_+}{\Gamma_0^2} K, \quad (23)$$

206 where the kernel K is

$$K(k_z) = (1 + \bar{k}_z M_\infty)^2 \Gamma_0 \left(\frac{J_l(k_0 \Gamma_0 a)}{J_l'(k_0 \Gamma_0 a)} - \frac{H_l^{(2)}(k_0 \Gamma_0 a)}{H_l^{(2)'}(k_0 \Gamma_0 a)} \right). \quad (24)$$

207 The functions will be factorised into analytic and non-analytic functions. Thus, factorise

208 K such that

$$K = \frac{K_+}{K_-} (\bar{k}_z - k_{z0})^2, \quad (25)$$

209 where K_+ and K_- are regular, and $k_{z0} = -k_0/M_\infty$. When substituted into Eq. (23) this gives

$$G_-(\bar{k}_z) K_-(\bar{k}_z) \Gamma_0^{-2} + G_+(\bar{k}_z) K_-(\bar{k}_z) \Gamma_0^{-2} = \frac{W_+(\bar{k}_z)}{\Gamma_0^{+2}} K_+(\bar{k}_z) (\bar{k}_z - k_{z0})^2. \quad (26)$$

210 Equation (26) is modified to ensure that the left hand side is regular in the lower-half plane,

$$\begin{aligned} G_-(\bar{k}_z) K_-(\bar{k}_z) \Gamma_0^{-2}(\bar{k}_z) + G_+(\bar{k}_z) K_-(\bar{k}_z) \Gamma_0^{-2}(\bar{k}_z) - \Gamma_0^{-2}(k_{z,lq}) K_-(k_{z,lq}) G_+(\bar{k}_z) = \\ \frac{W_+(\bar{k}_z)}{\Gamma_0^{+2}(\bar{k}_z)} K_+(\bar{k}_z) (\bar{k}_z - k_{z0})^2 - \Gamma_0^{-2}(k_{z,lq}) K_-(k_{z,lq}) G_+(\bar{k}_z). \end{aligned} \quad (27)$$

211 Then, using Liouville's theorem both sides of Eq. (27) are equal to a constant, say E . Let

212 $E(k_{z0}) = -\Gamma_0^{-2}(k_{z,lq}) K_-(k_{z,lq}) G_+(k_{z0})$ so that W_+ is given by

$$W_+(\bar{k}_z) = -\Gamma_0^{-2}(k_{z,lq}) \Gamma_0^{+2}(\bar{k}_z) \frac{K_-(k_{z,lq})}{K_+(\bar{k}_z) (k_0 - k_{z0})^2} [G_+(k_{z0}) - G_+(\bar{k}_z)]. \quad (28)$$

213 Using the method in Gabard and Astley ([14], Appendix A), the functions K_- and K_+ can

214 be evaluated. This gives

$$A(\bar{k}_z) = (1 + \bar{k}_z M_\infty)^2 \frac{W_+(\bar{k}_z)}{\Gamma_0^2 H_l^{(2)'}(k_0 \Gamma_0 a)}, \quad (29a)$$

$$B(\bar{k}_z) = (1 + \bar{k}_z M_\infty)^2 \frac{W_+(\bar{k}_z)}{\Gamma_0^2 J_l'(k_0 \Gamma_0 a)}. \quad (29b)$$

215 Thus, combining Eqs. (13) and (29), the transformed incident pressure field is given by

$$\tilde{p}_d(r, \bar{k}_z) = (1 + \bar{k}_z M_\infty)^2 \frac{W_+}{\Gamma_0} \begin{cases} \frac{H_l^{(2)}(k_0 \Gamma_0 r)}{H_l^{(2)'}(k_0 \Gamma_0 a)} & r > a \\ \frac{J_l(k_0 \Gamma_0 r)}{J_l'(k_0 \Gamma_0 a)} & r < a \end{cases}. \quad (30)$$

216 Only the incident field for $r > a$ will be required for the cylinder scattering problem. Thus,
217 the required field, for a spinning mode of amplitude P_{lq} , is expressed as

$$\tilde{p}_i(r, \bar{k}_z) = \tilde{p}_d(r, \bar{k}_z) = \tilde{\zeta}_{lq}(\bar{k}_z) H_l^{(2)}(k_0 \Gamma_0 r), \quad (31)$$

218 where

$$\tilde{\zeta}_{lq}(\bar{k}_z) = P_{lq} \frac{(1 + \bar{k}_z M_\infty)^2 W_+}{\Gamma_0 H_l^{(2)'}(k_0 \Gamma_0 a)}. \quad (32)$$

219 Then on taking the inverse Fourier transform, the incident field is given by

$$\hat{p}_i(r, \phi, z) = \frac{1}{2\pi} \int_{-\infty}^{\infty} \tilde{\zeta}_{lq}(\bar{k}_z) H_l^{(2)}(k_0 \Gamma_0 r) e^{-ik_0 \bar{k}_z z} d\bar{k}_z e^{-il\phi}. \quad (33)$$

220 The integration contour is deformed from the real axis by analytic continuation such that
221 the functions are regular. This means avoiding poles in K caused by the acoustic modes in
222 the duct. The location of the poles are the complex conjugate of those found in Ref. [14].

223 The key result is the complex amplitude of the incident field $\tilde{\zeta}_{lq}$ [Eq. (32)], which depends
224 on W_+ [Eq. (28)]. This is adapted from Gabard and Astley ([14], Eq. (3.22)). It is emphasised
225 that this is not a new result, since it gives the pressure field for a spinning duct mode radiated
226 from a cylindrical duct, but Eq. (31) is formulated so that the incident field can be combined
227 with the scattered field to determine the total field resulting from fuselage scattering.

228 C. Fuselage Scattering including Boundary-layer Refraction

229 Having determined the incident pressure for a spinning mode radiated from a circular duct
230 into a free field, the objective is to determine the total field in the presence of a cylindrical

231 fuselage located adjacent to the intake duct. The effect of refraction as the sound propagates
 232 through the fuselage boundary layer is included in the modelling.

233 The basic procedure now follows the method outlined in McAlpine et al. [10], with the
 234 method to include the boundary layer outlined in Gaffney et al. [11]. Graf's addition theorem
 235 ([10], Eq. (25)) is used to transform the incident field to the cylindrical polar coordinate
 236 system $(\bar{r}, \bar{\phi}, \bar{z})$ centred on the cylindrical fuselage. This transforms Eq. (33) to

$$\hat{p}_i(\bar{r}, \bar{\phi}, \bar{z}) = \frac{1}{(2\pi)^2} \sum_{n=-\infty}^{\infty} \left(\int_{-\infty}^{\infty} \tilde{p}_{i_n}(\bar{r}, \bar{k}_z) e^{-ik_0 \bar{k}_z \bar{z}} d\bar{k}_z \right) e^{-in\bar{\phi}}, \quad (34)$$

237 where

$$\tilde{p}_{i_n}(\bar{r}, \bar{k}_z) = 2\pi \tilde{\zeta}_{lq}(\bar{k}_z) (-1)^{(l+n)} e^{-i(l-n)\beta} \mathbf{H}_{l-n}^{(2)}(k_0 \Gamma_0 b) \mathbf{J}_n(k_0 \Gamma_0 \bar{r}). \quad (35)$$

238 It is important to note that $\tilde{\zeta}_{lq}(\bar{k}_z)$ is not affected by the transformation of coordinates.

239 The incident field is now defined. The method to incorporate fuselage scattering including
 240 boundary-layer shielding refraction now follows the same procedure outlined in Gaffney et
 241 al. ([11], Sec. II B).

242 An inviscid compressible isentropic perfect gas flow is assumed. The mean flow is assumed
 243 to be axisymmetric, parallel and directed in the negative axial direction, with constant mean
 244 density and sound speed profiles inside the boundary layer. The velocity profile M_z is given
 245 by

$$M_z = \begin{cases} M(\bar{r}) & 1 < \bar{r} \leq 1 + \delta \\ M_\infty & 1 + \delta < \bar{r} \end{cases}, \quad (36)$$

246 where δ is the non-dimensional thickness of the boundary-layer, and $M(\bar{r})$ is the boundary-
 247 layer Mach number profile. Note that the non-dimensional radius of the fuselage is unity.

248 Outside the boundary layer, where there is uniform flow, the acoustic pressure field is found

249 by solving the convected Helmholtz equation. In this region, each azimuthal component of
 250 the total pressure field can be expressed in the form

$$\tilde{p}_n(\bar{r}, \bar{k}_z) = \tilde{\eta}_n(\bar{k}_z) J_n(k_0 \Gamma_0 \bar{r}) + \tilde{\gamma}_n(\bar{k}_z) H_n^{(2)}(k_0 \Gamma_0 \bar{r}), \quad (37)$$

251 where $\tilde{\eta}_n(\bar{k}_z)$ and $\tilde{\gamma}_n(\bar{k}_z)$ are amplitude coefficients of the incident and cylindrical scattered
 252 waves respectively.

253 Inside the boundary-layer region, the acoustic pressure field will satisfy the Pridmore-
 254 Brown equation,

$$\left[\frac{d^2}{d\bar{r}^2} + \left(\frac{1}{\bar{r}} - \frac{2\bar{k}_z M'}{1 + \bar{k}_z M} \right) \frac{d}{d\bar{r}} + \left(k_0^2 \Gamma_0^2 - \frac{n^2}{\bar{r}^2} \right) \right] \tilde{p}_{bl_n} = 0, \quad (38)$$

255 where $M' = dM/d\bar{r}$.

256 There is no known analytical solution to the Pridmore-Brown equation, therefore a stan-
 257 dard Runge-Kutta ordinary differential solver is utilised. Accordingly, the transformed pres-
 258 sure in the boundary layer is normalised, i.e.

$$\tilde{p}_{bl_n}(\bar{r}, \bar{k}_z) = \tilde{\alpha}_n(\bar{k}_z) \tilde{f}_{bl_n}(\bar{r}, \bar{k}_z), \quad (39)$$

259 where \tilde{f}_{bl_n} is the normalised pressure, which is scaled by $\tilde{\alpha}_n(\bar{k}_z)$. On the surface of the rigid
 260 cylinder ($\bar{r} = a_0 = 1$), the boundary conditions are

$$\tilde{p}_{bl_n}(1, \bar{k}_z) = \tilde{\alpha}_n(\bar{k}_z) \quad \text{and} \quad \tilde{p}'_{bl_n}(1, \bar{k}_z) = 0. \quad (40)$$

261 The value of $\tilde{\alpha}_n$ must be proportional to the incoming wave. In order to formulate $\tilde{\alpha}_n$
 262 in terms of the incident wave amplitude, matching conditions are applied at the edge of the
 263 boundary layer ($\bar{r} = 1 + \delta$) to enforce continuity of pressure and the pressure gradient. The
 264 pressure in the boundary layer is scaled to match the amplitude of the incoming wave, i.e.

$$\tilde{\alpha}_n(\bar{k}_z) = \tilde{\Lambda}_n(\bar{k}_z) \tilde{\eta}_n(\bar{k}_z), \quad (41)$$

265 where

$$\tilde{\Lambda}_n(\bar{k}_z) = -\frac{2i}{\pi[1+\delta]} \frac{1}{\tilde{f}_{bl_n}\big|_{1+\delta} k_0\Gamma_0 H_n^{(2)'}(k_0\Gamma_0[1+\delta]) - \tilde{f}'_{bl_n}\big|_{1+\delta} H_n^{(2)}(k_0\Gamma_0[1+\delta])}, \quad (42)$$

266 and

$$\tilde{\eta}_n(\bar{k}_z) = 2\pi\tilde{\zeta}_{lq}(\bar{k}_z)(-1)^{(l+n)}e^{-i(l-n)\beta}H_{l-n}^{(2)}(k_0\Gamma_0 b). \quad (43)$$

267 It is noted that $\tilde{\Lambda}_n(\bar{k}_z)$ is a function that depends on the boundary-layer profile, but it does not
 268 depend on the spinning mode order (l, q) , whereas the amplitude coefficient $\tilde{\eta}_n(\bar{k}_z)$ depends
 269 on the spinning mode (l, q) , but it does not depend on the boundary-layer profile.

270 Finally, on the surface of the cylinder, the pressure can be calculated via

$$\hat{p}_t(a_0, \bar{\phi}, \bar{z}) = \frac{1}{(2\pi)^2} \sum_{n=-\infty}^{\infty} \left\{ \int_{-\infty}^{\infty} \tilde{\alpha}_n(\bar{k}_z) e^{-ik_0\bar{k}_z\bar{z}} d\bar{k}_z \right\} e^{-in\bar{\phi}}. \quad (44)$$

271 The integration contour of this solution is identical to that of the incident field, [Eq. (33)].

272 III. Validation

273 A. Implementation

274 Only brief details about the implementation procedure are mentioned in this article since
 275 similar details about the numerical implementation are given in the previous articles on this
 276 work by the authors [10],[11]. The Wiener–Hopf solution for a spinning mode has been
 277 implemented directly into the installation acoustics code by adapting another in-house code
 278 named ‘GXMunt’ written by Gwénaél Gabard, based on the formulation derived by Gabard
 279 and Astley [14].

280 The other difference between the new installation acoustics code, and the implementation
 281 described in Gaffney et al. [11], is that all wavenumbers in the Wiener–Hopf solution are taken

282 to be complex. This means that no special treatment is required for the critical layer in the
283 Pridmore-Brown equation, owing to this feature of the Wiener–Hopf solution. Consequently,
284 it is no longer necessary to implement a Frobenius solution to integrate the Pridmore-Brown
285 equation across the critical layer described in Gaffney et al. ([11], Sec. III). When imple-
286 menting the Wiener–Hopf method it is crucial to select an appropriate integration contour.
287 The integration path must ensure that all the split functions are regular, in order to apply
288 Cauchy’s integral theorem. This also applies to the inverse Fourier transform in Eq. (33),
289 where the contour is displaced from the real axis.

290 **B. Comparison between disc source and spinning mode source**

291 In order to verify the results from the new installation acoustics code, results are compared
292 between the disc source and the spinning mode source. Hocter [17] compared the Wiener–
293 Hopf solution for a spinning mode and an approximate result obtained by the Kirchhoff
294 approximation. The latter is directly comparable to the disk source model without the screen
295 utilised in previous work by the authors [10],[11]. Hocter showed a representative sample of
296 directivity patterns covering low- and high-order modes with a range of mode propagation
297 angles. In all these examples, the principal lobe was very similar in both predictions, but
298 all the directivity patterns were significantly different on approaching $\theta = 90^\circ$. It is not
299 possible to identify a single polar angle where the two solutions start to differ because Hocter
300 showed that it varied for different modes, but commonly the solutions differ starting at polar
301 angles between 60 and 70° . Since differences in the directivity between the Wiener–Hopf
302 solution for a spinning mode and the disk source model depend on the parameters which
303 define the spinning mode, a key benefit of using the Wiener–Hopf method is that it removes

304 this uncertainty by using a solution which is valid at all polar angles.

305 Figure 3 shows examples of the predicted sound pressure level on the cylindrical fuselage
306 at $\bar{\phi} = 0$ and $0 \leq \bar{z} \leq 2$. The pressure is calculated using the disc source or the spinning
307 mode source for the incident field. There is very close agreement between the two alternative
308 predictions in the range $1 \leq \bar{z} \leq 2$. Closer to the source plane, in the range $0 \leq \bar{z} \leq 1$, the
309 predictions differ, with typically a difference in excess of 5 dB at $\bar{z} = 0$. These predictions can
310 be used to estimate θ_{\max} , which corresponds to the maximum polar angle (measured as shown
311 in Fig. 1) at which there is good agreement between the fuselage pressure levels, predicted
312 by either the disc source or the spinning mode source. For the same parameters used with
313 Fig. 3, the values of θ_{\max} in Table 1 are calculated for a selection of values of \bar{z} , whereby the
314 value of \bar{z} specifies the axial location where the two alternative predictions (disc source and
315 spinning mode) start to diverge. It is seen in Fig. 3 that the two predictions typically start
316 to diverge in the range $0.5 \leq \bar{z} \leq 1$. This roughly corresponds to $\theta_{\max} \approx 70^\circ$, which is similar
317 to the findings in Hocter [17].

318 Figure 4 shows the predicted sound pressure levels on the whole cylindrical fuselage in the
319 range $-5 \leq \bar{z} \leq 5$ for an incident field comprised of a single mode, calculated using either
320 the disc source or the spinning mode source. This illustrates the region forward of the source
321 plane where predictions using either of the incident fields give very similar levels. In contrast,
322 closer to the source plane the predicted levels using the disc source are not realistic, because
323 in the absence of a mean flow the disc source prediction would be symmetric about the source
324 plane.

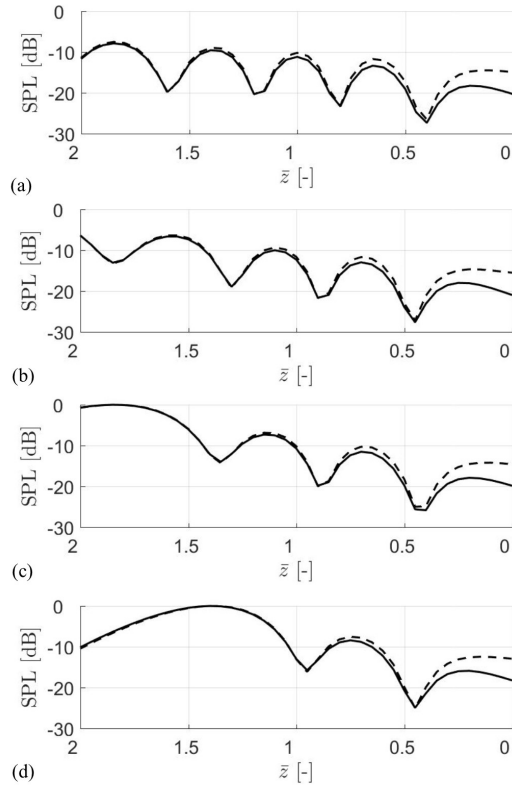


Figure 3: Predictions of the normalised SPL at $\bar{\phi} = 0$ for the disk source and spinning mode source. The mean flow is uniform with no boundary layer. The relevant parameters are $k_0 a = 20$, $a = 0.5$, $b = 3$ and $M_\infty = 0.75$. (a) $(l, q) = (4, 1)$, (b) $(l, q) = (11, 1)$, (c) $(l, q) = (14, 1)$ and (d) $(l, q) = (17, 1)$. Key: disk source (- - -); spinning mode (—).

Table 1: Estimates of θ_{\max} using the same parameters as in Fig. 3.

\bar{z} []	0.5	1.0	1.5	2.0
θ_{\max}	76°	63°	53°	45°

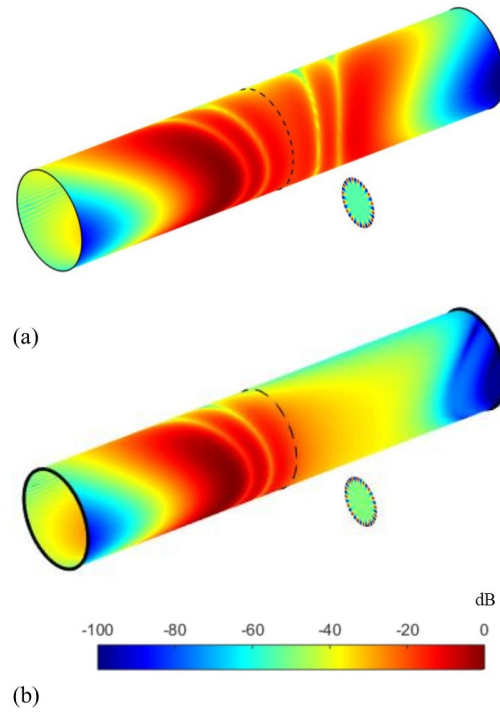


Figure 4: (Color online) Normalised total SPL on the cylinder. Comparison between the disc source (a) and the spinning mode source (b). The relevant parameters are $k_0 a = 20$, $a = 0.5$, $b = 3$, $(l, q) = (16, 1)$ and $M_\infty = 0.75$.

IV. Illustrative results

A. Boundary-layer shielding

This section focuses on the effect of boundary-layer refraction or ‘shielding’ on a single mode radiated from an intake duct. The difference between the predicted sound pressure level with and without the boundary layer, at a point on the cylindrical fuselage, is defined by

$$\Delta \text{ [dB]} = \text{SPL}_{bl} - \text{SPL} . \quad (45)$$

An example of Δ at $\bar{\phi} = 0$ and $-5 \leq \bar{z} \leq 5$ for a quarter-sine boundary layer is shown in Fig. 5. The Helmholtz number in these results is fixed at $k_0 a = 20$ (a realistic blade passing frequency), whilst the thickness of the boundary layer is varied from a very thin profile, $\delta = 0.0025$, to a thick profile, $\delta = 0.1$, as defined by 99% of the freestream velocity. For all the different boundary-layer thicknesses, there is little effect of boundary-layer refraction downstream of the source plane ($\bar{z} < 0$). However, upstream of the source ($\bar{z} > 0$), large reductions in the levels are predicted, caused by boundary-layer shielding as the upstream propagating sound is refracted away from the surface of the cylindrical fuselage. Even the very thin boundary-layer, $\delta = 0.0025$, is predicted to give a reduction of nearly 20 dB, compared to without the boundary layer, at $\bar{z} = 5$. This reduction in the predicted SPL increases as the thickness of the boundary layer is increased, and can lead to effectively total shielding with a thick boundary layer.

In order to quantify the effect of the boundary layer shielding over the whole cylinder, in Gaffney et al. [11] a simple shielding coefficient was introduced, defined by

$$S = \frac{(1/A) \int_A \overline{p_{bl}^2} dA}{(1/A) \int_A \overline{p^2} dA} \approx \frac{\sum^{\mathcal{M}} \overline{p_{bl}^2}}{\sum^{\mathcal{M}} \overline{p^2}} , \quad (46)$$

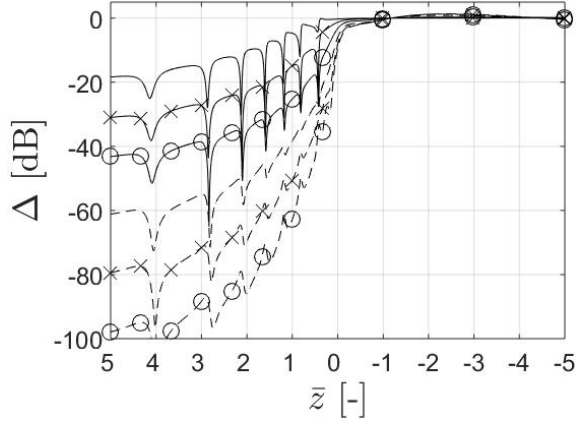


Figure 5: Predictions of Δ at $\bar{\phi} = 0$ for the spinning mode source. The boundary-layer profile is quarter-sine with boundary-layer thickness δ varying from 0.0025 to 0.1. The other relevant parameters are $(l, q) = (4, 1)$, $k_0 a = 20$, $a = 0.5$, $b = 3$, and $M_\infty = 0.75$. Key: $\delta = 0.0025$ (solid line, no symbols), $\delta = 0.01$ (solid line, \times), $\delta = 0.025$ (solid line, \circ), $\delta = 0.05$ (dashed line, no symbols), $\delta = 0.075$ (dashed line, \times), $\delta = 0.1$ (dashed line, \circ).

344 where in practice it is sufficient to evaluate S via a sum of the predicted mean square pressures
 345 over the \mathcal{M} grid points distributed over the cylinder surface. The value of S will be between
 346 0 and 1, where zero represents total shielding and unity represents no shielding.

347 However, in the previous work there were only simulation results upstream of the source
 348 plane. Therefore in order to examine the effects of upstream and downstream sound propa-
 349 gation, additional shielding coefficients S_+ and S_- are defined

$$S_+ = \frac{\sum_{\mathcal{M}_+} \overline{p_{bl}^2}}{\sum_{\mathcal{M}_+} \overline{p^2}} \Big|_{\bar{z} > 0} \quad \text{and} \quad S_- = \frac{\sum_{\mathcal{M}_-} \overline{p_{bl}^2}}{\sum_{\mathcal{M}_-} \overline{p^2}} \Big|_{\bar{z} < 0}, \quad (47)$$

350 where $\mathcal{M}_{+/-}$ denotes the grid points distributed over the cylinder's surface for $\bar{z} \gtrless 0$. It is
 351 emphasised that $S \neq S_+ + S_-$.

352 An illustrative result is shown in Fig. 6 with the same parameters used in the example shown
 353 in Fig. 5. In Fig. 6(a) the S_+ and S_- shielding coefficients are plotted against boundary-layer

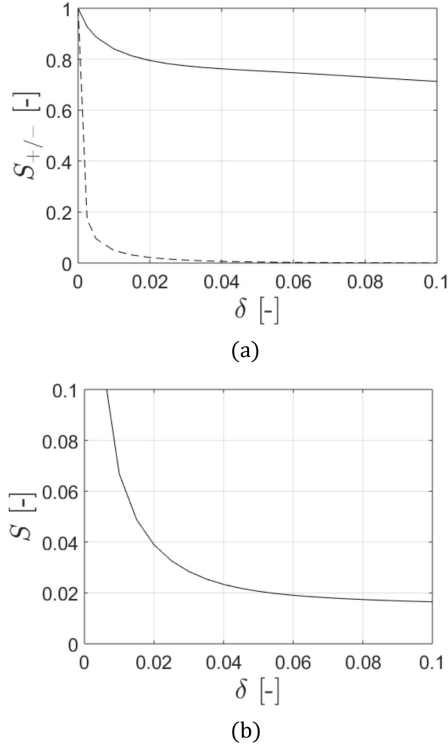


Figure 6: Prediction of the shielding coefficient S for the quarter-sine boundary layer profile with varying boundary-layer thickness δ : (a) S_+ (dashed line) and S_- (solid line); (b) S .

The relevant parameters are $(l, q) = (4, 1)$, $k_0 a = 20$, $a = 0.5$, $b = 3$ and $M_\infty = 0.75$.

354 thickness from $\delta = 0$ to 0.1. This isolates the upstream and downstream effects of boundary-
 355 layer refraction. For upstream propagating sound only a relatively thin boundary layer is
 356 required for very significant shielding to be predicted. For downstream propagating sound
 357 some modest shielding is predicted, but in fact this is due to the difference in the predictions
 358 on the far side of the cylinder (not shown). In Fig. 6(b) the total shielding over the whole
 359 cylinder (upstream and downstream combined) is very significant, even for thin boundary
 360 layers, owing to the shielding of sound propagating upstream of the source plane.

B. Multi-mode simulations

In Gaffney et al. [11] the illustrated results showing the effect of boundary-layer shielding were for a single incident mode. However, a multi-mode source provides a better representation of fan tone radiation. This section presents some multi-mode results.

From Sec. II.C, the surface pressure \hat{p}_t [Eq. (44)] is expressed in terms of an inverse Fourier transform of the function $\tilde{\alpha}_n(k_z)$ [Eq. (41)], where $\tilde{\alpha}_n$ is the product of the functions $\tilde{\Lambda}_n(k_z)$ [Eq. (42)] and $\tilde{\eta}_n(k_z)$ [Eq. (43)]. The evaluation of $\tilde{\Lambda}_n$ is the principal time-consuming step in the method, since it involves the numerical integration of the Pridmore-Brown equation through the boundary layer. However, $\tilde{\Lambda}_n$ is independent of the incident mode order (l, q) ; only the function $\tilde{\eta}_n$ is dependent on (l, q) . This means that multi-mode results can be calculated very efficiently, because for a fixed frequency the function $\tilde{\Lambda}_n(k_z)$ is only required to be evaluated once. For the simulation results shown in this section, an incoherent sum of all the cut-on modes is performed, but despite the incoherent sum involving 127 modes, the total run-time is only around twice the computation time that is required for a single mode.

The simulation results shown in Fig. 7 are for a multi-mode source with equal power per (cut-on) mode, whereas in Fig. 7 the results are for a multi-mode source with equal power per mode, except mode $(l, q) = (16, 1)$ which is 45 dB higher. This type of scenario reflects the situation where one or more modes may be dominant owing to the type of source mechanism, for example, rotor-locked modes which are dominant when the rotor-locked pressure field is cut on.

In both examples, the total SPL on the surface of the cylinder is shown for the range $-5 \leq \bar{z} \leq 5$. At $\bar{z} = 5$, with the thin boundary-layer the predicted SPL is approximately

383 20 dB less than is predicted with uniform flow (no boundary layer). With the thick boundary-
384 layer the predicted SPL is approximately 50 dB less compared with no boundary layer. These
385 reductions are due to the boundary-layer refracting the sound away from the cylinder, and,
386 as expected, the effect of boundary-layer shielding is much more significant with the thick
387 boundary layer.

388 Contrastingly, downstream of the source plane the predicted levels with uniform flow or
389 the thin boundary layer are very similar. There are small differences compared with the thick
390 boundary-layer, but, also as expected, the effect of boundary-layer shielding is rather small,
391 since the downstream propagating sound is refracted towards the cylinder.

392 Finally, in Fig. 8 the directivity pattern of mode $(l, q) = (16, 1)$ is visible, mapped onto
393 the surface of the cylinder. The intersection of the principal lobe corresponds to the area of
394 highest SPL. Overall, the results in Fig. 8 are very similar to the results in Fig. 7, but with
395 the effective directivity pattern of the protruding mode imposed on the visualisations of the
396 total sound pressure levels.

397 **V. Discussion**

398 Nayfeh et al. [18] showed that inside a flow duct, predictions quantifying the effect of boundary-
399 layer shielding showed similar results for different boundary-layer profiles if the different pro-
400 files were scaled such that they had the same displacement thickness (δ^*). The exception was
401 the power-law profile which is commonly used to model a turbulent boundary layer.

402 A similar illustrative example is shown in Fig. 9, based on the exterior problem considered
403 in the present work, i.e. boundary-layer shielding on the external surface of a cylindrical

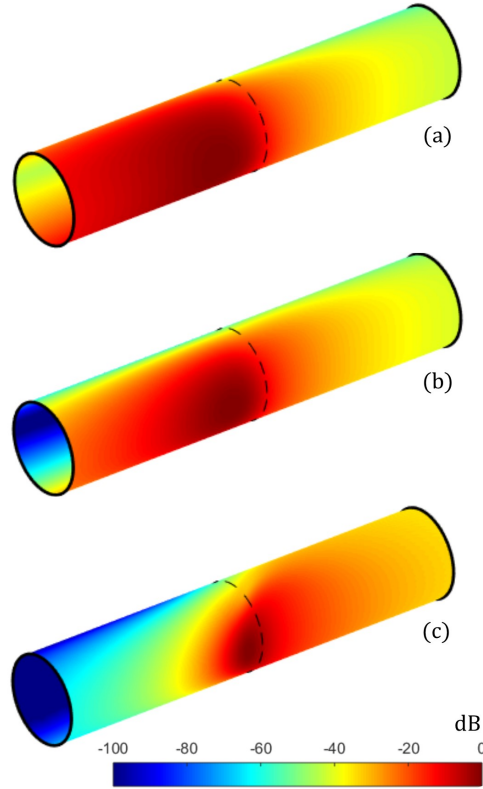


Figure 7: (Color online) Normalised total SPL on the surface of the cylinder for an incoherent, multi-mode source with equal power per mode: (a) uniform flow, $\delta = 0.0$; (b) $\delta = 0.01$; and (c) $\delta = 0.1$. The boundary-layer profile is quarter-sine. The dashed line shows the position of the source plane $\bar{z} = 0$ (the source is not shown). The relevant parameters

are $k_0 a = 20$, $a = 0.5$, $b = 3$ and $M_\infty = 0.75$.

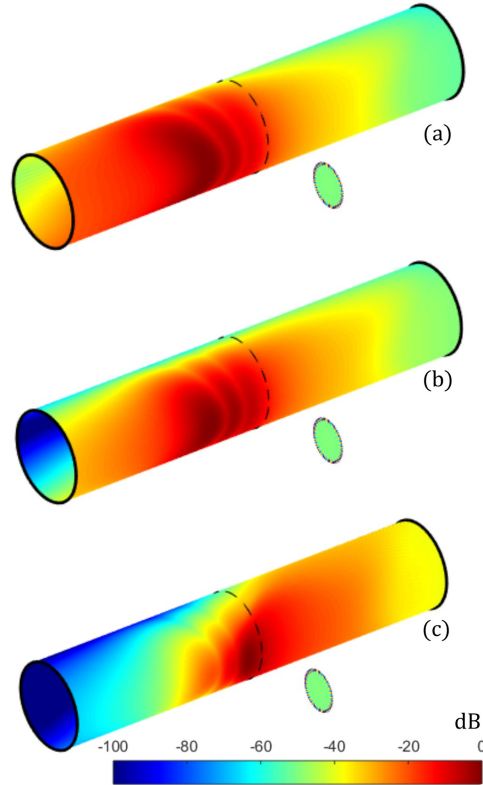


Figure 8: (Color online) Normalised total SPL on the surface of the cylinder for an incoherent, multi-mode source with equal power per mode except $(l, q) = (16, 1)$ whose modal amplitude is set 45 dB higher: (a) uniform flow, $\delta = 0.0$; (b) $\delta = 0.01$; and (c) $\delta = 0.1$. The boundary-layer profile is quarter-sine. The dashed line shows the position of the source plane $\bar{z} = 0$. The relevant parameters are $k_0 a = 20$, $a = 0.5$, $b = 3$ and $M_\infty = 0.75$.

404 fuselage. Predictions of Δ [Eq. (45)] for three boundary-layer profiles are compared. The
 405 profiles are linear, quarter-sine and 1/7th power law with linear sublayer of thickness 0.001δ .
 406 The results show predictions of Δ versus δ^* at two different locations on the fuselage. The
 407 range of δ^* from zero to 0.0125 is equivalent to varying the boundary-layer thickness δ from
 408 zero to 0.1 for the 1/7th power-law profile. In Fig. 9 it is seen that at both locations on
 409 the cylinder, the predictions of Δ obtained with the linear or quarter-sine profiles are almost
 410 identical, but the predictions with the power-law profile differ from the other two profiles.
 411 This is consistent with the previous findings reported by Nayfeh et al. for the flow duct
 412 problem.

413 Also in Fig. 9, the results clearly show that for thin boundary layers the rate-of-change
 414 of Δ is nonlinear as δ^* is increased, whereas for thicker boundary layers the change in Δ is
 415 linearly proportional to the change in δ^* .

416 It is possible to predict similar values of Δ obtained with the power-law profile by utilising
 417 a simple, discontinuous, ‘step’ velocity profile. The ‘step’ velocity profile is taken to be zero
 418 for $0 < \bar{r} < 1 + \tau\delta$, and equal to M_∞ for $1 + \tau\delta < \bar{r}$, where δ is the thickness of the power-
 419 law boundary layer. There is a discontinuous step change in the velocity from zero to the
 420 free-stream value at $\bar{r} = 1 + \tau\delta$. Predictions of Δ versus δ for the 1/7th power-law boundary-
 421 layer profile, and the ‘step’ velocity profile with $\tau = \frac{1}{3}$, are shown in Fig. 10. Results are
 422 compared at locations upstream ($\bar{z} = 5$), downstream ($\bar{z} = -5$) and in the source plane
 423 ($\bar{z} = 0$). There is excellent agreement between the two separate predictions of Δ upstream of
 424 the source, where shielding will be very significant. Thus, it is seen that the ‘step’ velocity
 425 profile (with an appropriate value of τ) could be used instead of the power-law profile to
 426 calculate realistic predictions of boundary-layer shielding. The benefit of this approach is

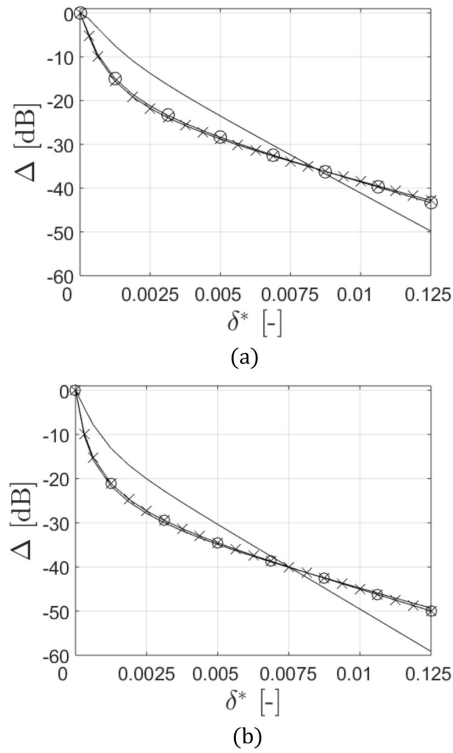


Figure 9: Predictions of Δ versus boundary-layer displacement thickness δ^* for three different velocity profiles. The 1/7th power-law boundary layer is compared against linear and quarter-sine boundary-layer profiles at (a) $\bar{\phi} = 0$, $\bar{z} = 0$, and, (b) $\bar{\phi} = 0$, $\bar{z} = 5$. The relevant parameters are $(l, q) = (4, 1)$, $k_0 a = 20$, $a = 0.5$, $b = 3$ and $M_\infty = 0.75$. Key: power-law (solid line); linear (solid, \times); quarter-sine (solid, \circ).

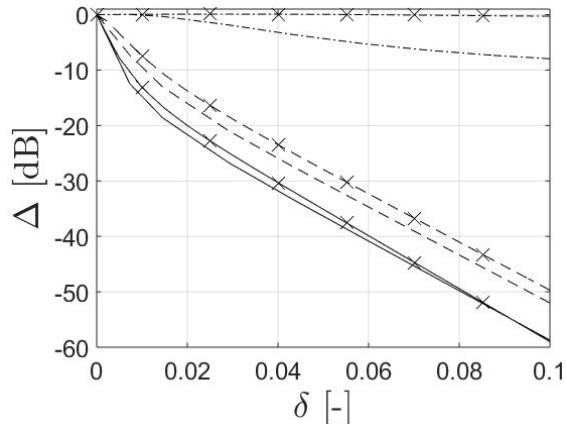


Figure 10: Predictions of Δ versus boundary-layer thickness δ for two different velocity profiles. The 1/7th power-law boundary layer is compared against the step-change profile, with step thickness equal to one-third of the boundary-layer thickness. Results are shown at $\bar{\phi} = 0$ and $\bar{z} = 5, 0,$ and -5 . The relevant parameters are $(l, q) = (4, 1)$, $k_0 a = 20$, $a = 0.5$, $b = 3$ and $M_\infty = 0.75$. Key: $\bar{z} = 5$ (solid lines); $\bar{z} = 0$ (dashed lines); $\bar{z} = -5$ (dashed-dot lines); power-law (crosses), and step-change (no symbol).

427 that a fully analytical solution can be derived for a ‘step’ velocity profile because there is
 428 no sheared flow. Consequently, the calculations are extremely quick, comparable with the
 429 calculations for uniform flow with no fuselage boundary layer.

430 VI. Conclusions

431 In this article, the key advancement to a theoretical model for calculating the fuselage pressure
 432 levels due to fan tones radiated from the intake of an installed turbofan aero-engine is the
 433 use of a Wiener–Hopf solution of a spinning mode exiting a cylindrical duct to specify the
 434 incident field. As in previous work by the authors [10, 11], the total field is given by the sum
 435 of the incident and scattered fields, and is calculated with the inclusion of refraction by the

436 fuselage boundary layer. The advanced method enables more representative predictions to
437 be obtained in the region around the source plane, up to a maximum polar angle $\theta_{\max} > 90^\circ$,
438 after which point the intake fan noise ceases to be the dominant source of noise incident on the
439 fuselage.

440 This work focusses on the prediction of intake fan tones, such as “buzz-saw” tones, and
441 the incident sound on the fuselage forward of the wings. However, the radiation of bypass
442 fan tones also is applicable using the Wiener–Hopf technique, and has been examined by
443 a number of authors including Munt [16], Rienstra [19], Gabard and Astley [14], Samanta
444 and Freund [20] and Veitch and Peake [21]. Thus there is scope to use the Wiener–Hopf
445 method to construct the incident field for a fan tone radiated from the bypass duct, and to
446 incorporate this into the installation acoustics method. However this problem has significant
447 added complexity, compared to the intake noise radiation problem. Other tonal sources,
448 such as turbine tones, are radiated from the engine’s exhaust. Sound radiated from the
449 exhaust propagates through the jet shear layers which causes refraction, and also, potentially,
450 spectral broadening or ‘haystacking’ of tonal sound fields. Additionally for the installation
451 acoustics problem, exhaust noise radiation will be affected by the wings for wing-mounted
452 engines. Thus, for incident sound on the fuselage downstream of the wings, there are number
453 of additional issues that would need to be examined. Recently the current focus of research in
454 this area has focussed on the issue of jet-wing interaction, which could be a more significant
455 source of the aft noise radiation.

456 Illustrative results show that boundary-layer shielding forward of the source can be very
457 significant. It is also highlighted that it is possible to obtain realistic estimates of the shield-
458 ing without necessarily modelling the realistic boundary-layer profile. It may be sufficient

459 to ensure that the profile has realistic thickness parameters, without necessarily having to
460 determine the realistic mean-flow profile.

461 It is also shown that multi-mode sources can be simulated very efficiently using this ap-
462 proach, without any prohibitive increase in the computational cost compared to simulations
463 for a single mode.

464 In summary, the fidelity of this theoretical model for installation acoustics is comparable
465 with previous methods which had been developed for propeller noise sources, but not for
466 turbofan noise sources. The incident field can be calculated using the Wiener–Hopf solution
467 which is valid at all polar angles, thus predictions can be extended downstream as well as
468 upstream of the source plane. However, it is emphasised that further downstream the fuselage
469 pressure levels will be dominated by exhaust noise sources.

470 All the data supporting this study is openly available from the University of Southampton
471 repository at <http://dx.doi.org/10.5258/SOTON/XXXXXX>

472 **Acknowledgements**

473 The authors wish to thank Gwénaél Gabard who kindly provided the Wiener–Hopf code
474 ‘GXMunt’ for use in this work, and for informative discussions on the theory that he had
475 developed in a previous article (Gabard and Astley [14]).

476 Also the authors wish to acknowledge the continuing financial support provided by Rolls-
477 Royce plc through the University Technology Centre in Gas Turbine Noise at the Institute of
478 Sound and Vibration Research. The first author also acknowledges the financial contribution
479 from the EPSRC via the University of Southampton’s DTP grant.

References

- [1] J. Bowman, T. Senior, and P. Uslenghi, eds., *Electromagnetic and Acoustic Scattering by Simple Shapes* (North-Holland Publishing Co. – Amsterdam) (1969).
- [2] G. McAninch, “A note on propagation through a realistic boundary layer”, *Journal of Sound and Vibration* **88**, 271–274 (1983).
- [3] D. Hanson, “Shielding of prop-fan cabin noise by the fuselage boundary layer”, *Journal of Sound and Vibration* **92**, 591–598 (1984).
- [4] D. Hanson and B. Magliozzi, “Propagation of propeller tone noise through a fuselage boundary layer”, *Journal of Aircraft* **22**, 63–70 (1985).
- [5] H. Lu, “Fuselage boundary-layer effects on sound propagation and scattering”, *American Institute of Aeronautics and Astronautics Journal* **28**, 1180–1186 (1990).
- [6] I. Belyaev, “The effect of an aircraft’s boundary layer on propeller noise”, *Acoustical Physics* **58**, 425–433 (2012).
- [7] H. Brouwer, “The scattering of open rotor tones by a cylindrical fuselage and its boundary layer”, *Proceedings of the 22nd AIAA/CEAS Aeroacoustics conference*, Lyon, France, AIAA paper no. 2016-2741 16 pp. (30 May–1 June, 2016).
- [8] M. Siefert and J. Delfs, “Refraction and scattering in high Mach number boundary layers”, AIAA 2011-2847 (2011), *Proceedings of the 17th AIAA/CEAS Aeroacoustics Conference*, Portland, Oregon, June 5–8, 9 pages.

- 499 [9] J. Dierke, R. Ewert, J. Delfs, C. Stoehr, and M. Rose, “The effect of a boundary layer on
500 engine noise propagating to the fuselage at flight conditions”, AIAA 2013-2006 (2013),
501 Proceedings of the 19th AIAA/CEAS Aeroacoustics Conference, Berlin, Germany, May
502 27–29, 14 pages.
- 503 [10] A. McAlpine, J. Gaffney, and M. Kingan, “Near-field sound radiation of fan tones from
504 an installed turbofan aero-engine”, Journal of the Acoustical Society of America **138**,
505 131–1324 (2015).
- 506 [11] J. Gaffney, A. McAlpine, and M. Kingan, “Fuselage boundary-layer refraction of fan
507 tones radiated from an installed turbofan aero-engine”, Journal of the Acoustical Society
508 of America **141**, 1653–1663 (March 2017), <http://dx.doi.org/10.1121/1.4976965>.
- 509 [12] J. Tyler and T. Sofrin, “Axial flow compressor noise studies”, SAE Transactions **70**,
510 309–332 (1962).
- 511 [13] G. Homicz and J. Lordi, “A note on the radiative directivity patterns of duct acoustic
512 modes”, Journal of Sound and Vibration **41**, 283–290 (1975).
- 513 [14] G. Gabard and R. Astley, “Theoretical model for sound radiation from annular jet pipes:
514 far- and near-field solutions”, Journal of Fluid Mechanics **549**, 315–341 (2006).
- 515 [15] Gabard and Astley define time-harmonic waves using the convention $\exp\{-i\omega_0 t\}$ and
516 take the duct radius a as the reference lengthscale. In the current article, the convention
517 used for time-harmonic waves is $\exp\{i\omega_0 t\}$ and the reference lengthscale is the cylinder
518 radius a_0 .

- 519 [16] R. Munt, “The interaction of sound with a subsonic jet issuing from a semi-infinite
520 cylindrical pipe”, *Journal of Fluid Mechanics* **83**, 609–640 (1977).
- 521 [17] S. Hocter, “Exact and approximate directivity patterns of the sound radiated from a
522 cylindrical duct”, *Journal of Sound and Vibration* **227**, 397–407 (1999).
- 523 [18] A. Nayfeh, J. Kaiser, and B. Shaker, “Effect of mean-velocity profile shapes on sound
524 transmission through two-dimensional ducts”, *Journal of Sound and Vibration* **34**, 413–
525 423 (1974).
- 526 [19] S. W. Rienstra, “Acoustic radiation from a semi-infinite annular duct in a uniform sub-
527 sonic mean flow”, *Journal of Sound and Vibration* **94**, 267–288 (1984).
- 528 [20] A. Samanta and J. Freund, “Finite-wavelength scattering of incident vorticity and acous-
529 tic waves at a shrouded-jet exit”, *Journal of Fluid Mechanics* **612**, 407–438 (2008).
- 530 [21] B. Veitch and N. Peake, “Acoustic propagation and scattering in the exhaust flow from
531 coaxial cylinders”, *Journal of Fluid Mechanics* **613**, 275–307 (2008).

532 List of Figures

533	1	Canonical problem for intake fan tone radiation from an installed turbofan	
534		aero-engine. (a) Sketch of an installed turbofan aero-engine mounted below	
535		the wings. (b) Incident field = disk source. (c) Incident field = Spinning	
536		mode. Polar angle θ_{\max} indicates, along with the shaded regions, roughly where	
537		predictions of the fuselage pressure levels are valid.	7
538	2	(Color online) Sketch of the cylindrical fuselage (radius a_0) and the circular	
539		intake duct (radius a). The centreline of the cylinder is aligned with the \bar{z} -	
540		axis. The intake duct is aligned with the z -axis, and the duct termination is	
541		located in the plane $z = \bar{z} = 0$. The transverse distance between the centre of	
542		the intake duct and the centre of the cylinder is b . Also shown is the edge of	
543		the fuselage boundary-layer (thickness δ).	8
544	3	Predictions of the normalised SPL at $\bar{\phi} = 0$ for the disk source and spinning	
545		mode source. The mean flow is uniform with no boundary layer. The relevant	
546		parameters are $k_0 a = 20$, $a = 0.5$, $b = 3$ and $M_\infty = 0.75$. (a) $(l, q) = (4, 1)$, (b)	
547		$(l, q) = (11, 1)$, (c) $(l, q) = (14, 1)$ and (d) $(l, q) = (17, 1)$. Key: disk source (-	
548		- -); spinning mode (—).	21
549	4	(Color online) Normalised total SPL on the cylinder. Comparison between the	
550		disc source (a) and the spinning mode source (b). The relevant parameters are	
551		$k_0 a = 20$, $a = 0.5$, $b = 3$, $(l, q) = (16, 1)$ and $M_\infty = 0.75$	22

552	5	Predictions of Δ at $\bar{\phi} = 0$ for the spinning mode source. The boundary-layer	
553		profile is quarter-sine with boundary-layer thickness δ varying from 0.0025 to	
554		0.1. The other relevant parameters are $(l, q) = (4, 1)$, $k_0a = 20$, $a = 0.5$, $b = 3$,	
555		and $M_\infty = 0.75$. Key: $\delta = 0.0025$ (solid line, no symbols), $\delta = 0.01$ (solid line,	
556		\times), $\delta = 0.025$ (solid line, \circ), $\delta = 0.05$ (dashed line, no symbols), $\delta = 0.075$	
557		(dashed line, \times), $\delta = 0.1$ (dashed line, \circ).	24
558	6	Prediction of the shielding coefficient S for the quarter-sine boundary layer	
559		profile with varying boundary-layer thickness δ : (a) S_+ (dashed line) and S_-	
560		(solid line); (b) S . The relevant parameters are $(l, q) = (4, 1)$, $k_0a = 20$,	
561		$a = 0.5$, $b = 3$ and $M_\infty = 0.75$	25
562	7	(Color online) Normalised total SPL on the surface of the cylinder for an in-	
563		coherent, multi-mode source with equal power per mode: (a) uniform flow,	
564		$\delta = 0.0$; (b) $\delta = 0.01$; and (c) $\delta = 0.1$. The boundary-layer profile is quarter-	
565		sine. The dashed line shows the position of the source plane $\bar{z} = 0$ (the source	
566		is not shown). The relevant parameters are $k_0a = 20$, $a = 0.5$, $b = 3$ and	
567		$M_\infty = 0.75$	28
568	8	(Color online) Normalised total SPL on the surface of the cylinder for an in-	
569		coherent, multi-mode source with equal power per mode except $(l, q) = (16, 1)$	
570		whose modal amplitude is set 45 dB higher: (a) uniform flow, $\delta = 0.0$; (b)	
571		$\delta = 0.01$; and (c) $\delta = 0.1$. The boundary-layer profile is quarter-sine. The	
572		dashed line shows the position of the source plane $\bar{z} = 0$. The relevant param-	
573		eters are $k_0a = 20$, $a = 0.5$, $b = 3$ and $M_\infty = 0.75$	29

574	9	Predictions of Δ versus boundary-layer displacement thickness δ^* for three	
575		different velocity profiles. The 1/7th power-law boundary layer is compared	
576		against linear and quarter-sine boundary-layer profiles at (a) $\bar{\phi} = 0$, $\bar{z} = 0$,	
577		and, (b) $\bar{\phi} = 0$, $\bar{z} = 5$. The relevant parameters are $(l, q) = (4, 1)$, $k_0 a = 20$,	
578		$a = 0.5$, $b = 3$ and $M_\infty = 0.75$. Key: power-law (solid line); linear (solid, \times);	
579		quarter-sine (solid, \circ).	31
580	10	Predictions of Δ versus boundary-layer thickness δ for two different velocity	
581		profiles. The 1/7th power-law boundary layer is compared against the step-	
582		change profile, with step thickness equal to one-third of the boundary-layer	
583		thickness. Results are shown at $\bar{\phi} = 0$ and $\bar{z} = 5$, 0, and -5 . The relevant	
584		parameters are $(l, q) = (4, 1)$, $k_0 a = 20$, $a = 0.5$, $b = 3$ and $M_\infty = 0.75$. Key:	
585		$\bar{z} = 5$ (solid lines); $\bar{z} = 0$ (dashed lines); $\bar{z} = -5$ (dashed-dot lines); power-law	
586		(crosses), and step-change (no symbol).	32